ARC Alliance

ARC Geophysical Research

GR Geophysical Research

Phase-Resolved Shear Stress and Sediment Flux Profiles in a Combined Wave-Current Bottom Boundary Layer

Galen Egan*[1]

[1]Geosciences Department, Princeton University, Princeton, NJ, USA

Abstract

Phase-resolved profiles of shear stress and turbulent sediment flux were collected in the wave bottom boundary layer of South San Francisco Bay. Observations revealed a transitional boundary layer influenced by benthic roughness, which modified the phase variability and vertical structure of the wave-induced velocity and shear stress compared to classic laboratory experiments. The phase relationship between free stream velocity and bed shear stress was, on average, close to that oberseved in previous studies. Wave friction factor measurements were evaluated against various parameterizations, finding that the Gon et al. [16] and Rogers et al. [35] formulations were most accurate. The Grant and Madsen [18] combined wave-current shear stress model accurately predicted the total bed shear stress, though negative bias increased with wave strength. Finally, turbulent sediment fluxes exhibited complex vertical structure, but were consistently driven by a mix of bed shear stress and the horizontal wave pressure gradient. These results provide important validation for popular bottom boundary layer models, while highlighting the complexities of cohesive sediment erosion over rough beds and in combined wave-current forcing.

Keywords: Bed Shear Stress, Wave-Current Interaction, Erosion

1 Introduction

In estuaries and coastal regions, hydrodynamics and sediment transport are strongly influenced by interactions with the bottom boundary; therefore, numerical models of these systems

*Corresponding Author
E-mail address: gegan@princeton.edu
doi 10.5149/ARC-GR.1704

must accurately represent the bed shear stress [14]. This coupling can be seen from the governing momentum balance, which can be written following e.g., Grant and Madsen [18], as

$$\frac{\partial \boldsymbol{u}}{\partial t} = -\frac{1}{\rho_0}\nabla_H p + \frac{\partial}{\partial z}\left(\frac{\boldsymbol{\tau}}{\rho_0}\right). \tag{1}$$

Here, $\boldsymbol{u} = (u(z,t), v(z,t))$ is the horizontal fluid velocity which varies with height z and time t, ∇_H is the horizontal gradient operator in the x and y directions, p is the pressure, ρ_0 is the assumed constant fluid density, $\boldsymbol{\tau} = (\tau_x(z,t), \tau_y(z,t))$ is the shear stress, and we have neglected both Coriolis effects and convective acceleration. Each component of velocity can be further decomposed as

$$u = \underbrace{\overline{u} + u'}_{u_c} + \underbrace{\tilde{u}}_{u_w} \tag{2}$$

where u_c is the component due to the steady, turbulent current with time average $\overline{u}$ and fluctuations u', and u_w is the component due to surface gravity waves. We similarly decompose the pressure $p = p_c + p_w$.

Our goal in this work will be to measure the terms in Equation 1 as directly as possible using *in situ* observations from the shallow mudflats of South San Francisco Bay, where both waves and tidal currents contribute to the shear stress and resulting sediment transport [3]. From these observations, we will characterize the shear stress associated with (a) the wave-driven flow (which we denote $\boldsymbol{\tau_w}$), and (b) the combined wave-current flow ($\boldsymbol{\tau}$). These observations will be compared to common parameterizations for wave-induced and combined wave-current shear stress. We will also explore the phasing between near-bed velocity $\boldsymbol{u}$ and stress $\boldsymbol{\tau}$, and examine sediment resuspension in the context of these fluid dynamics.

2 Methods

2.1 Field Deployment

The dataset that we collected and our observational methods have been described in other publications [6, 8–10]. We refer the reader to those manuscripts for full details, and summarize the most relevant information here for clarity.

We deployed a fixed instrument platform at 37.58745 N, 122.18530 W in South San Francisco Bay from 07/17/2018– 08/15/2018 (Figure 1). The study site was located at 1.5 m mean lower low water, with a 2 m tidal range. Tidal currents ran approximately northwest/southeast during ebb/flood respectively, with a maximum depth-averaged current magnitude of 33 cm/s. Northwesterly winds picked up each afternoon, driving eastward-propagating wind waves with bottom wave-orbital velocities over 10 cm/s and peak periods ranging from 0.25–0.6 Hz.

The platform contained Nortek Vector Acoustic Doppler Velocimeters (ADVs) with measurement volumes at 5, 15, and 45 cm above the bed. Each ADV collected co-located pressure and 3D velocity at 8 Hz for a 14 minute burst period each hour. The platform also contained an RBR Bottom Pressure Recorder (BPR), which sampled pressure continuously at 6 Hz for the duration of the deployment. We additionally deployed a Nortek Vectrino Profiler with its 30 mm tall measurement volume overlapping the bed, resulting in 3D velocity and acoustic backscatter measurements over 1 mm vertical bins from 0 - 1.4 cm above the bed. The Vectrino sampled at 64 Hz for 12 minutes each hour, centered on the 14 minute ADV burst periods.

Adjacent to the fixed platform, we also collected sediment cores from the study site. Laboratory disaggregated particle size distribution measurements revealed a fine-grained cohesive bed with median primary particle size $d_{50} = 8$ μm. On top of the sediment, each core contained a dense mat of feeding tubes built by the benthic worm *Sabaco elongatus* and amphipod

Figure 1: Deployment site in South San Francisco Bay. Black arrows denote the direction of the ebb and flood tidal currents, while the red arrow denotes the mean direction of the wind waves.

Ampelisca abdita. As described in Egan et al. [8] and Egan et al. [9], the enhanced roughness from these benthic features had a profound influence on the structure of the near-bed flow. Consideration of the unique bed geometry in the analyses carried out in this manuscript are further detailed in Section 3.2.1.

2.2 Data Processing

Velocity observations were rotated into an east-north (x-y) coordinate system, aligning with the eastward wave propagation direction at the study site. Each burst sample was despiked using a phase-space method [17]. The full velocity signal was then decomposed into wave-driven and turbulent components $\tilde{u}$ and u' following Cowherd et al. [6], which adapts the Bricker and Monismith [4] method to allow for recovery of decomposed velocity time series, as opposed to bulk spectral statistics. Wave phase θ was identified via Hilbert Transform of $\tilde{u}(z_p)$, the potential wave velocity in the Vectrino bin furthest from the bed ($z_p = 1.4$ cm).

Bulk wave statistics were estimated using a mix of instrumentation. The potential wave orbital velocity magnitude was calculated from Vectrino data as

$$u_0 = \sqrt{\mathrm{var}\left(\tilde{u}(z_p)\right) + \mathrm{var}\left(\tilde{v}(z_p)\right)}. \tag{3}$$

This definition is consistent with Madsen [28], neglecting the factor of $\sqrt{2}$ that is sometimes used [44]. To validate that $z_p = 1.4$ cm was representative of potential flow conditions, we compared u_0 estimates from the Vectrino and the nearby ADV sampling at 5 cm above the bed. These two estimates showed excellent agreement, with $r^2 = 0.97$, root-mean-squared error 0.39 cm/s, and a mean bias -0.07 cm/s. This negative bias indicates that the Vectrino slightly underpredicted u_0 due to its close proximity to the bed, but given that the average wave orbital velocity was ≈ 5 cm/s over the deployment period, we can assume that the Vectrino data in its top measurement bin gave a reasonable approximation of the potential flow velocity.

Once u_0 was estimated, we restricted our dataset to time periods where $u_0 > 1.5$ cm/s, as we found that bulk wave statistics (in particular wave period) were noisy below that cutoff. Wave direction was estimated from ADV data [19]. The radian wave frequency ω was estimated from the peak frequency in the pressure power spectral density measured by the BPR. The BPR was also used to measure total water depth H.

Bottom roughness was examined for this study site in detail, finding tidal asymmetry in drag coefficient and associated bottom roughness z_0 due to heterogeneity in the benthic feeding tube canopies [9]. Therefore, it is an open question as to whether the flood tide bottom roughness, ebb tide bottom roughness, an average of the two, or a tidally-dependent roughness is most appropriate for the friction felt by waves. From testing these options, we found that the flood tide value produced the best agreement with the parameterizations that we evaluate (Section 3.3). This may be because waves at the study site propagate in nearly the same direction as the flooding tide. We therefore use a representative physical (Nikuradse) bottom roughness value $k_b = 30z_0 = 0.645$ cm, the average flood tide value estimated from the 5 and 15 cm above bed ADVs (0.66 ± 0.09 cm and 0.63 ± 0.11 cm, respectively, [9, Figure 2 therein]).

Vectrino data within the bottom boundary layer was also available for estimating bottom roughness, though the value reported by Egan et al. [9] (0.15 ± 0.04 cm) was significantly lower than both ADV estimates. This discrepancy has two potential sources: (1) the authors vertically-averaged the Vectrino Reynolds stresses, including data from the region where stresses began to decay towards zero, and (2) near-bed turbulent stress was shown to be reduced by sediment-induced stratification [10]. However, the log profile assumption required for mapping a drag coefficient to k_b should still be valid at the ADV heights: laboratory experiments by Vallikivi et al. [43] found a log layer upper bound at approximately 0.15δ, where δ is the channel half-height. Using $\delta = 0.75$ m (half the mean lower low water), the 5 cm ADV would always fall below 0.15δ, and the 15 cm ADV would fall below 0.15δ for water depths 2 m or greater (95% of the time). Considering both the uncertainty in the Vectrino roughness estimate due to stratification, and the general agreement between the two ADV estimates, the ADV k_b values were deemed more reliable. The sensitivity of our results to the precise choice of k_b will be further discussed in Section 3.1.

Suspended sediment concentration c was estimated from the acoustic backscatter amplitude of the Vectrino, using previously reported calibrations [10]. This allowed for calculation of turbulent sediment flux profiles from the covariance $\overline{c'w'}$, where w' is the fluctuating vertical turbulent velocity.

2.3 Shear Stress Estimation

2.3.1 Theoretical Considerations

First we consider the purely wave-driven flow where $\boldsymbol{u} = \boldsymbol{u_w}$:

$$\frac{\partial \boldsymbol{u_w}}{\partial t} = -\frac{1}{\rho_0}\nabla_H p_w + \frac{\partial}{\partial z}\left(\frac{\boldsymbol{\tau_w}}{\rho_0}\right) \tag{4}$$

Outside the wave boundary layer, frictional effects are negligible, and the wave pressure gradient is given by

$$-\frac{1}{\rho_0}\nabla_H p_w = \frac{\partial \boldsymbol{u_p}}{\partial t}, \tag{5}$$

where $\boldsymbol{u_p}$ is the potential flow velocity. Substituting Equation 5 into Equation 4,

$$\frac{\partial}{\partial t}\left(\boldsymbol{u_w} - \boldsymbol{u_p}\right) = \frac{\partial}{\partial z}\left(\frac{\boldsymbol{\tau_w}}{\rho_0}\right). \tag{6}$$

Integrating from the potential flow region at z_p (where the wave stress is zero) to an arbitrary z produces an expression for the wave shear stress:

$$\boldsymbol{\tau_w}(z) = \rho_0 \int_{z_p}^{z} \frac{\partial}{\partial t}\left(\boldsymbol{u_w} - \boldsymbol{u_p}\right) \mathrm{d}z, \tag{7}$$

which is the velocity defect form of the shear stress commonly found in the literature [13, 20, 24].

Next we follow an analogous procedure for the combined wave-current flow. Expanding the full momentum equation produces:

$$\frac{\partial \boldsymbol{u_w}}{\partial t} + \frac{\partial \boldsymbol{u_c}}{\partial t} = -\frac{1}{\rho_0}\nabla_H p_w - \frac{1}{\rho_0}\nabla_H p_c + \frac{\partial}{\partial z}\left(\frac{\boldsymbol{\tau}}{\rho_0}\right). \tag{8}$$

The second term on the left-hand side is negligible, and we can substitute Equation 5 for the first term on the right-hand side. The second term on the right-hand side (pressure gradient associated with the steady current) was not directly measured during our study. However, we did measure the bottom stress associated with the current, and in steady, turbulent open-channel flow, it is reasonable to assume that the pressure gradient is balanced by bottom friction. In the x-direction,

$$-\frac{\partial p_c}{\partial x} = \frac{\partial \tau_x}{\partial z} \tag{9}$$

Assuming that the pressure is hydrostatic and that the shear stress decreases linearly from $\rho_0 u_*^2$ at the bed to zero at the surface, we can integrate over the depth H to obtain:

$$-\frac{1}{\rho_0}\frac{\partial p_c}{\partial x} = \frac{u_*^2}{H} \tag{10}$$

Defining the friction velocity in terms of the Reynolds stress associated with the turbulent current $\boldsymbol{u_*}^2 = (-\overline{u'w'}, -\overline{v'w'})\,|_{z=0}$, substituting into Equation 8, and rearranging, we obtain

$$\frac{\partial}{\partial t}\left(\boldsymbol{u_w} - \boldsymbol{u_p}\right) - \frac{\boldsymbol{u_*}^2}{H} = \frac{\partial}{\partial z}\left(\frac{\boldsymbol{\tau}}{\rho_0}\right). \tag{11}$$

Integrating from z_p to an arbitrary z,

$$\boldsymbol{\tau}(z) - \boldsymbol{\tau}(z_p) = \rho_0 \int_{z_p}^{z} \left(\frac{\partial}{\partial t}\left(\boldsymbol{u_w} - \boldsymbol{u_p}\right) - \frac{\boldsymbol{u_*}^2}{H}\right) \mathrm{d}z. \tag{12}$$

We once again invoke the linear stress distribution and make the substitution

$$\boldsymbol{\tau}(z_p) = \rho_0 \boldsymbol{u_*}^2 \left(1 - \frac{z_p}{H}\right) \tag{13}$$

to obtain

$$\boldsymbol{\tau}(z) = \rho_0 \left(\boldsymbol{u_*}^2 \left(1 - \frac{z_p}{H}\right) + \int_{z_p}^{z} \left(\frac{\partial}{\partial t}\left(\boldsymbol{u_w} - \boldsymbol{u_p}\right) - \frac{\boldsymbol{u_*}^2}{H}\right) \mathrm{d}z\right). \tag{14}$$

It is straightforward to validate that at $z = z_p$, Equation 14 reduces to Equation 13. Moreover, under wave-free conditions, we recover $\boldsymbol{\tau}(z = 0) = \rho_0 \boldsymbol{u_*}^2$, and in a purely wave-driven flow we recover Equation 7.

2.3.2 Estimating shear stress from Vectrino data

With profiles of wave velocity isolated, we evaluated the phase- and height-varying wave stress using Equation 7, averaging over eight equally-spaced phase bins from $\theta = [-180°, 180°]$. In addition to the directional stress components, we evaluated the total wave shear stress as

$$|\boldsymbol{\tau_w}| = \sqrt{\tau_{w,x}^2 + \tau_{w,y}^2} \tag{15}$$

With the measured wave shear stress, we can further estimate a wave friction factor f_w, which is commonly used to parameterize the maximum shear stress the bed feels over a wave cycle with

$$\tau_{wm} = \frac{1}{2}\rho_0 f_w u_0^2. \tag{16}$$

From the Vectrino $|\boldsymbol{\tau_w}|$, we can extract a maximum value $|\boldsymbol{\tau_{wm}}|$ over the vertical coordinate and all discretized wave phases for each measurement burst period (the precise height at which we allow the maximum to be defined requires some nuance, which will be further discussed in Section 3.2). This leads to a Vectrino-derived wave friction factor

$$f_w = \frac{2|\boldsymbol{\tau_{wm}}|}{\rho u_0^2}. \tag{17}$$

To evaluate the combined wave-current shear stress (Equation 14), we estimated the squared friction velocity based on the Reynolds stress in the potential flow region, i.e.,

$$\boldsymbol{u_*^2} = \left(\frac{-\overline{u'w'}(z = z_p)}{\left(1 - \frac{z_p}{H}\right)}, \frac{-\overline{v'w'}(z = z_p)}{\left(1 - \frac{z_p}{H}\right)} \right), \tag{18}$$

and analogous to the wave case, define the total combined wave-current shear stress

$$|\boldsymbol{\tau}| = \sqrt{\tau_x^2 + \tau_y^2} \tag{19}$$

2.3.3 Shear Stress Parameterizations

As a comparison to the measured wave and combined wave-current shear stresses, we evaluate a number of theoretical formulations and empirical parameterizations that have been proposed. For the pure wave case, this includes the laminar limit wave friction factor [23]:

$$f_w = \frac{2}{\sqrt{Re_w}}, \tag{20}$$

where Re_w is the wave Reynolds number given by

$$Re_w = \frac{a_b^2 \omega}{\nu}, \tag{21}$$

with $a_b = u_0 \omega^{-1}$ the bottom wave-orbital excursion amplitude and $\nu = 1 \times 10^{-6}$ m^2/s the assumed constant kinematic viscosity of water. For rough turbulent wave boundary layers, most parameterizations are based on the relative roughness a_b/k_b. We examine the Kamphuis parameterization [25]:

$$\frac{1}{4\sqrt{f_w}} + \log_{10}\left(\frac{1}{4\sqrt{f_w}}\right) = -0.35 + \frac{4}{3}\log_{10}\left(\frac{a_b}{k_b}\right); \tag{22}$$

the Jonsson parameterization [23]:

$$\frac{1}{4\sqrt{f_w}} + \log_{10}\left(\frac{1}{4\sqrt{f_w}}\right) = -0.08 + \log_{10}\left(\frac{a_b}{k_b}\right); \tag{23}$$

and three parameterizations that all take the form:

$$f_w = \exp\left(a_1 \left(\frac{a_b}{k_b}\right)^{a_2} + a_3\right). \tag{24}$$

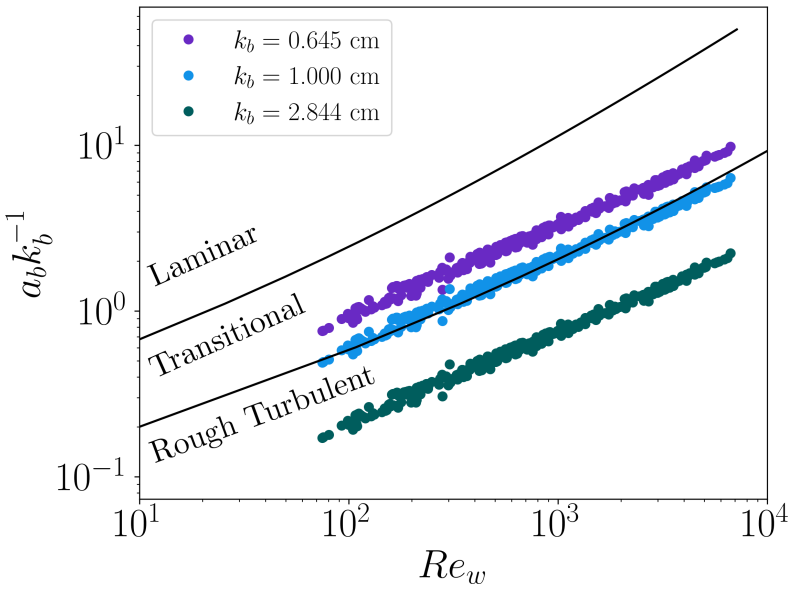

Figure 2: Relative roughness as a function of wave Reynolds number for three different bottom roughness values (markers). Solid lines indicate boundaries between different wave boundary layer flow regimes [25, Equations 13 and 14 therein].

These correspond to Nielsen [33], Rogers et al. [35], and Grant and Madsen [18] (hereafter GM), with fit coefficients (a_1, a_2, a_3) = (5.5, -0.2, -6.3), (5.213, -0.194, -5.977), and (7.02, -0.078, -8.82), respectively. In the range of relative roughness examined here, the Rogers et al. [35] parameterization is equivalent to the earlier formulation of Swart [42]; we will refer to it as the Rogers parameterization for simplicity.

Finally, we considered a more recent parameterization by Gon et al. [16] that was developed using data over a rocky shoreline. However, their formulation relied on a standard deviation roughness height σ_b rather than a Nikuradse roughness k_b, taking the form

$$f_w = 1.94 \left(\frac{a_b}{\sigma_b} \right)^{-0.97} . \tag{25}$$

To address this difference, we defined $\sigma_b = \alpha k_b$ and fit an optimal value of α using our measured wave friction factor and assumed bottom roughness k_b. This produced an optimal $\alpha = 0.258$. Recast as $k_b = \alpha^{-1}\sigma_b$, our result of $\alpha^{-1} \approx 3.88$ is consistent with previous studies that have found $k_b = 4\sigma_b$ [27, 39].

For the combined wave-current flow, we compare our maximum (over the vertical coordinate and all wave phases) combined wave current shear stress $|\boldsymbol{\tau_m}|$ to the parameterizations of GM and Styles [18, 41]. These models both produce a combined wave-current shear stress $\rho_0 u_{*cw}^2$, but the latter is designed for arbitrarily large bed roughness.

3 Results and Discussion

3.1 Boundary Layer Regime

A wave bottom boundary layer can be classified as either laminar, transitional, or turbulent based on its relative roughness and wave Reynolds number [25]. Following Lacy and MacVean [26], Figure 2 shows our dataset in $a_b k_b^{-1} - Re_w$ space for three k_b values.

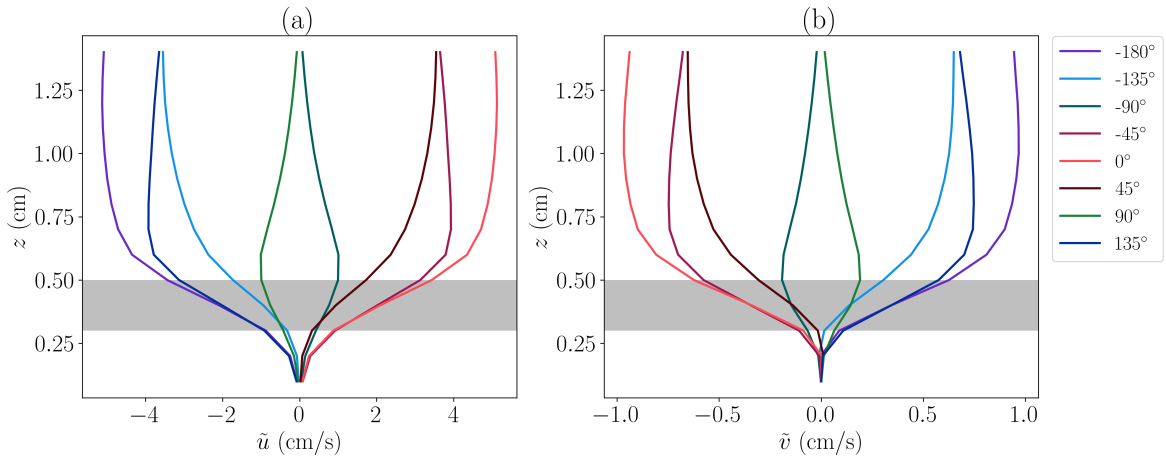

Figure 3: Phase-resolved velocity profiles in the (a) x-direction and (b) y-direction, ensemble-averaged over all measurement bursts during the deployment period. The shading highlights the beginning of the logarithmic portion of the profile, informing our definition of the bed for purposes of estimating the bed shear stress (Equation 26)

At the roughness $k_b = 0.645$ cm that we assume for the remainder of the manuscript, the boundary layer is classified as transitional for the entire range of Reynolds numbers that we observed. Therefore, we would not expect a laminar wave friction factor (Equation 20) to accurately represent the bottom friction. However, some of the purely turbulent formulations may not be appropriate either (see Section 3.3.2). If we had used the ebb tide value $k_b = 2.844$ cm from Egan et al. [9], the bottom boundary layer would be fully turbulent, while a representative value of $k_b = 1.0$ cm that one might use in the absence of observations would fall nearly on the boundary between transitional and turbulent. Given that any of these three values could be justifiable, this analysis highlights the sensitivity of the boundary layer regime (and resulting parameterized shear stress) to the choice of bottom roughness.

3.2 Mean Velocity

Though already presented for this dataset by Cowherd et al. [6], it is necessary to replicate the phase-resolved wave velocity profiles in order to highlight the peculiar bottom roughness conditions. This, in turn, will allow us to define a "bed" height z_b where the bed shear stress is calculated, and enable comparison to classic oscillatory boundary layer laboratory experiments.

3.2.1 Canopy Flow Characteristics and Bed Definition

Figure 3 shows the x- and y-components of the phase-averaged wave velocity profiles. Because waves were primarily aligned in the x-direction, the remainder of our analysis will focus on the u component of velocity and stress along with the total (vector sum) stress magnitude, with the goal of comparing our high-resolution *in situ* observations to similar laboratory experiments and commonly-used bottom stress parameterizations. However, the vertical structure of the velocity profiles in Figure 3 complicate that goal: as discussed by Egan et al. [8], flexible benthic feeding tubes induced a near-bed flow more akin to a dense canopy mixing layer with its characteristic hyperbolic tangent structure [31] than the flat-plate boundary layer (and logarithmic law of the wall structure) assumed by the stress parameterizations we wish to evaluate. Nepf [32] discusses the difficulty of defining a bed shear stress within dense canopies:

both the viscous stress and Reynolds stresses go to zero at the sediment bed, which could imply that $\boldsymbol{\tau}(z=0) \approx 0$. On the other hand, integration of the velocity defect (Equation 7) would indicate a monotonically increasing stress towards $z = 0$. The true bed stress is likely somewhere in between, and requires consideration of the spatially-averaged drag associated with individual canopy elements [31, 32]. We unfortunately have no reliable way to estimate that drag with the data we collected.

However, this inability to estimate the stress at $z = 0$ need not spoil the entire analysis because it is reasonable to define our "bed" as the inflection point where the velocity profile can be approximated as logarithmic, thus mimicking the structure of the laboratory velocity profiles and the profile that is assumed in the parameterizations we compare results to [18, 41]. The stress at that location defines the bottom drag felt by the tidal flow and the waves, and is therefore the most relevant quantity for hydrodynamic modeling applications. And while it is not as coupled to sediment transport as the true bed stress at $z = 0$, it is likely correlated (see Egan et al. [11] for an erosion analysis of this dataset). Quantitatively, we defined the "bed" location for each measurement burst period as the height where the mean velocity gradient was maximized. Across the deployment, this varied between $z \approx 0.3-0.5$ cm (shaded region in Figure 3). With this in mind, we introduce more specific definitions of our measured maximum bed stresses for the wave-driven and combined wave-current flow during each measurement burst period:

$$\boldsymbol{\tau_{wm}} = \max_{\theta} \langle \boldsymbol{\tau_w}(\theta, z) \rangle \tag{26a}$$

$$\boldsymbol{\tau_m} = \max_{\theta} \langle \boldsymbol{\tau}(\theta, z) \rangle, \tag{26b}$$

where $\langle\rangle$ denotes a vertical average between $z = 0.3 - 0.5$ cm.

3.2.2 Comparison with Laboratory Profiles of Wave Velocity

One of the first sets of phase-resolved wave bottom boundary layer measurements in the laboratory was presented by Jonsson and Carlsen [24] (hereafter JC76), who published data tables of their velocity and shear stress profiles for two trials, which we transcribed for replication here. While their observations were at much higher $Re_w \approx 10^6$ and $a_b k_b^{-1} \approx 10^2$, it is worth comparing our results in terms of phase behavior and vertical structure. To better compare the profiles, we normalize the wave velocity during each burst period by u_0, and normalize the vertical coordinate by $\delta_w = u_* \omega^{-1}$, a scaling for the wave boundary layer thickness, where $u_* = (\tau_{wm,x} \rho_0^{-1})^{1/2}$. In our dataset, we also offset the vertical coordinate by $\delta_c = 0.4$ cm (the mean bed location). This offset ensures that the field profiles begin in the logarithmic region rather than the canopy region, which is neccesary for comparitive purposes because the JC76 data have no canopy flow characteristics. Figure 4 shows this comparison, with Figure 4a depicting the wave velocity averaged over all measurement burst periods ($u_0 > 1.5$ cm/s), and 4a depicting Trial 1 from JC76.

Qualitatively, the velocity profiles in Figures 4a and 4b have similar phasing but significantly different vertical structure. Analyzing the phase variability more quantitatively, Figure 5 shows the potential and near-bed velocities for the field and laboratory data as a function of wave phase, with the velocity data reprocessed using 15° phase bins rather than 45°. We then fit a cubic spline to each set of observations to enhance the resolution in phase lag estimates. In the field observations (Figure 5a), the maximum potential flow velocity $\tilde{u}_p$ is 18.0° out of phase with the maximum near-bed velocity $\tilde{u}_b$. This contrasts with the laboratory data, where the maxima are lagged by $\Delta\theta = 33.2°$.

The closer phase alignment in the field observations suggests more efficient downward momentum transport as compared to the laboratory data, perhaps as a consequence of the

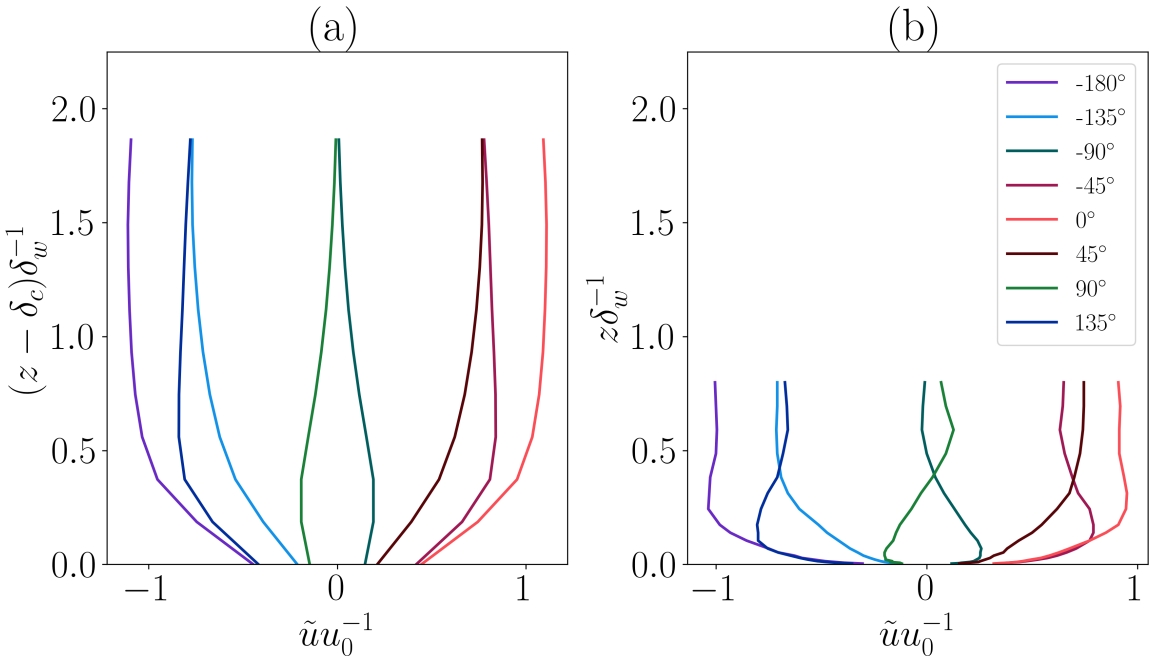

Figure 4: A comparison of phase-resolved mean velocity profiles between (a) Vectrino data ensemble-averaged across the deployment and (b) laboratory velocity profiles of Jonsson and Carlsen [24].

rough benthic canopy in the field. In a similar vein, while the laboratory profiles show a thin boundary layer reaching $\approx 0.25\delta_w$ and distinct "overshoot" region at all phases, the field observations appear more diffuse with a boundary layer thickness nearing $\approx 0.5 - 0.75\delta_w$.

To further probe the differences in boundary layer height between the field and lab, we estimated a wave boundary layer height based on a displacement thickness approach [37]

$$\delta_\theta = \int_0^{z_m} \left(1 - \frac{|\tilde{u}(z)|}{\max(|\tilde{u}(z)|)}\right), \tag{27}$$

where z_m is the height corresponding to $\max(|u(z)|)$, the maximum absolute value of the velocity profile during the wave phase with the highest vertically-averaged velocity magnitude. Consistent with Cowherd et al. [6], we scale the displacement thickness to define the boundary layer height as $2\delta_\theta$. We then examined the nondimensional boundary layer height $2\delta_\theta/\delta_w$ (i.e., measured boundary layer height normalized by the turbulent wave boundary layer height scaling) as a function of relative roughness $a_b k_b^{-1}$ for the field observations, along with both of the trials reported in JC76. This analysis is shown in Figure 6.

The trend in Figure 6 indicates that the differences in vertical structure between the field and lab observations may be controlled by relative roughness: for $a_b k_b^{-1} \sim \mathcal{O}(1)$, the boundary layer height approaches $u_*\omega^{-1}$ with an $\mathcal{O}(1)$ scale factor, while in the limit of $a_b k_b \gg 1$, the boundary layer height approaches $\sim 0.01 u_*\omega^{-1}$. The two sets of observations fall between these limits. A proposed exponential fit in the same form as the parameterizations for wave friction factor (e.g., Equation 24) fit the bin-averaged field data and laboratory observations with $r^2 = 0.87$. At present, most wave bottom boundary layer models assume that the boundary layer thickness is proportional to $u_*\omega^{-1}$ with a constant scale factor (the precise factor ranges from $\sim 0.15 - 0.8$ depending on the study [5, 18, 21, 45]). Therefore, our parameterization could serve as a useful generalization by incorporating roughness variability into the scaling relationship.

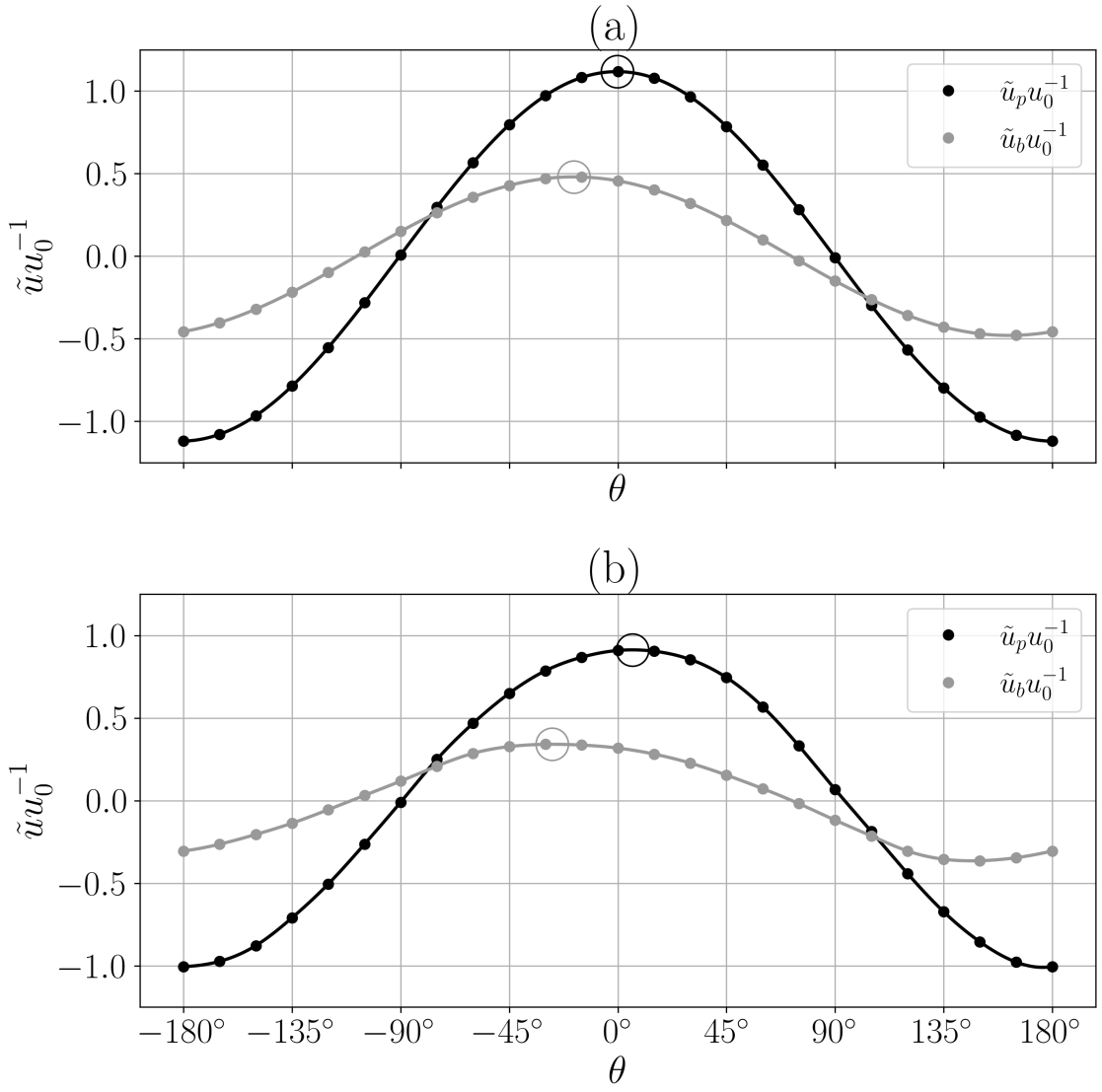

Figure 5: Potential wave velocity (black solid markers) and wave velocity at the bed (gray solid markers) normalized by u_0 for the (a) field observations and (b) JC76 laboratory observations. Spline fits are plotted as lines, and the maximum value for each variable is denoted by the large open marker, with the phase lag defined as the phase difference between maximum values.

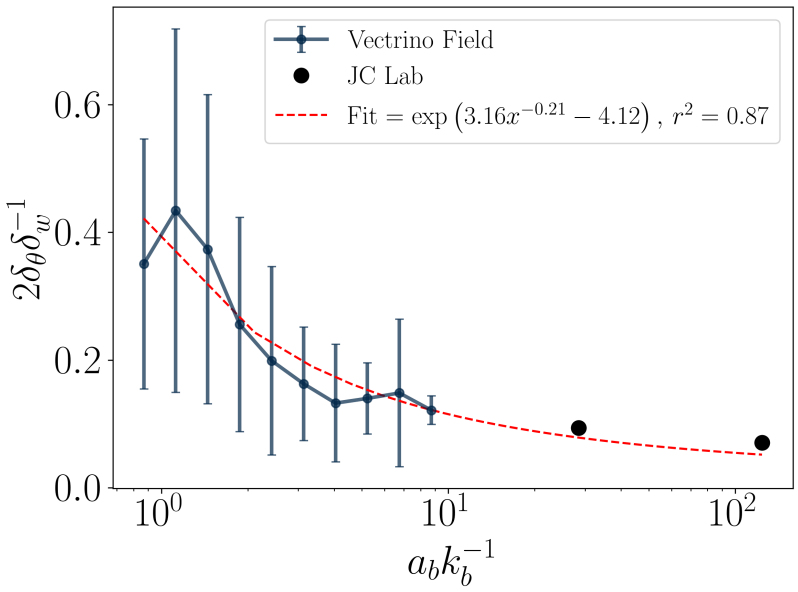

Figure 6: Normalized boundary layer height as a function of relative roughness for both the field observations (markers with error bars) and the two JC76 trials (markers), along with a best-fit curve (red dashed line).

In summary, we found qualitative similarities between the field and laboratory wave bottom boundary layer velocity profiles. This agreement lends confidence to our wave-turbulence decomposition and phase-averaging procedures, and suggests that velocity defect laws (Equations 7 and 14) will be appropriate for estimating stress from the velocity profiles. Additionally, differences between the two sets of observations can likely be explained by differences in the roughness regime, with higher roughness in the field leading to a thicker boundary layer and reduced vertical phase variability.

3.3 Shear Stress

3.3.1 Comparison with Laboratory Profiles of Wave Stress

Figure 7 depicts vertical profiles of wave shear stress (Equation 7) in our dataset and JC76 Trial 1. Similar to the velocity, strong stresses were confined to a thinner boundary layer in the lab compared to the field; we again attribute this difference to the enhanced roughness at the field site.

To more quantitatively analyze phase variability between the field and lab shear stress data, we next examined the phase difference between the potential velocity $\tilde{u}_p$ and the wave-induced shear stress at the bed, $\langle \tau_{w,x} \rangle$. The relative phasing of these two quantities is important for sediment dynamics, as the stress is responsible for resuspending sediment from the bed while the velocity dictates transport [36]. In laminar theory (i.e., Stokes second problem), the stress leads the velocity by $\Delta\theta = 45°$ [2]. In a turbulent wave boundary layer, however, laboratory studies have shown a gradual decrease in phase lead with increasing wave Reynolds numbers [13, 40]. More recently, laboratory experiments and direct numerical simulations showed that the phase difference can change signs (i.e., the velocity leads the stress) in transitional boundary layers [15, 30]. Our dataset provides a unique opportunity to compare those results to *in situ* field observations.

For this analysis, we used the same 15° phase increment dataset as in Figure 5, with a

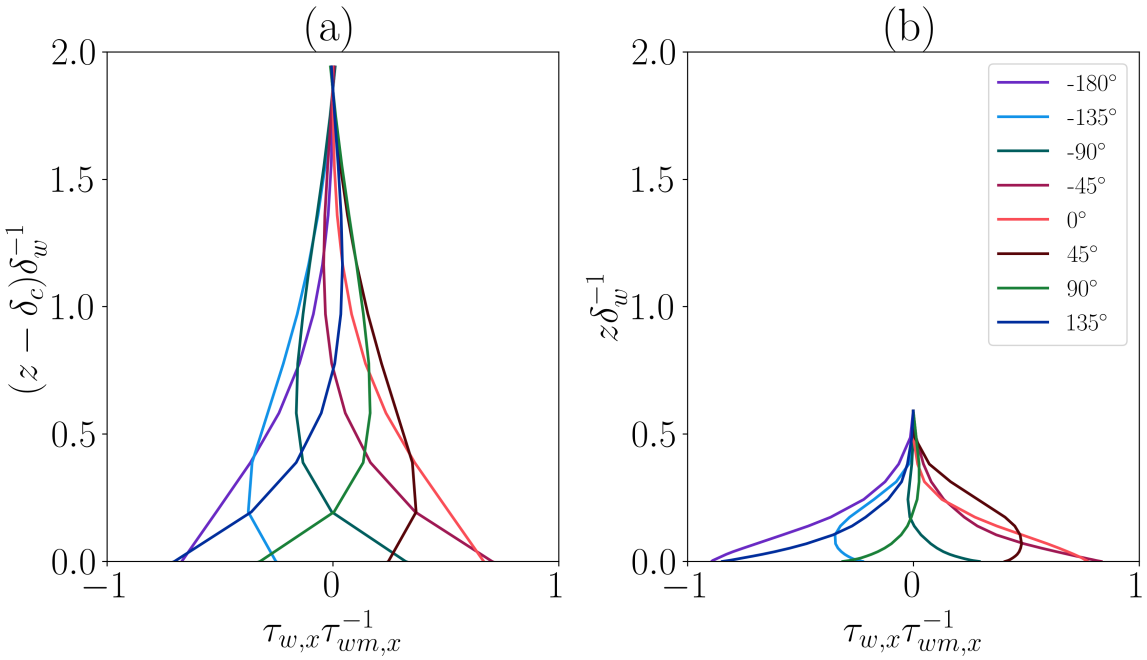

Figure 7: A comparison of phase-resolved wave shear stress profiles between (a) Vectrino data (Equation 7) ensemble-averaged across the deployment, and (b) laboratory velocity profiles of JC76 Trial 1. The stress is normalized by $\tau_{wm,x}$ in each burst period prior to ensemble-averaging.

similar spline fitting procedure to estimate the phase lag. Results for the average velocity and stress profiles are shown in Figure 8a, which had a phase lag $\Delta\theta = 31.7°$. This is closer to the laminar value than the JC76 study, which has a phase lag of 23.4°. Considering the relatively low wave Reynolds number range in our dataset ($Re_w < 10^4$), a phase lag closer to the laminar value is consistent with prior work [30].

Beyond the mean phase lag, we also examined the velocity-stress phase lag for individual measurement bursts to check for instances of "reversed" lags where the velocity led the stress. This reversal, consistent with behavior seen in other transitional wave boundary layers [15, 30], occurred in approximately 20% of the measurement bursts. However, other individual bursts had phase lags $|\Delta\theta| > 45°$, i.e., larger than the laminar limit. Unfortunately, we were unable to identify any consistent physical factor driving those spurious phase lags, so we restrict our analysis to the deployment-averaged lag (Figure 8).

3.3.2 Wave Friction Factor Parameterizations

Figure 9 shows our calculated wave friction factor (Equation 17) as a function of relative roughness, along with each of the parameterizations that we evaluate. As expected, the laminar formulation tends to underestimate f_w across the range of $a_b k_b^{-1}$. The turbulent formulations tend to converge for $a_b k_b^{-1} \gg 1$, but diverge significantly in the lower relative roughness regime. For example, the turbulent formulation of Kamphuis [25] significantly overestimates f_w, producing a similar RMSE as the laminar estimate. GM generally underestimates f_w and has the highest error of all the parameterizations. Nielsen [33] and Rogers et al. [35] are nearly identical with impressive low RMSE; Jonsson [23] is similar but suffers from its prescribed maximum of $f_w = 0.3$. The parameterization with lowest RMSE is Gon et al. [16], with the caveat that it relied on an optimal fit coefficient mapping bottom roughness height

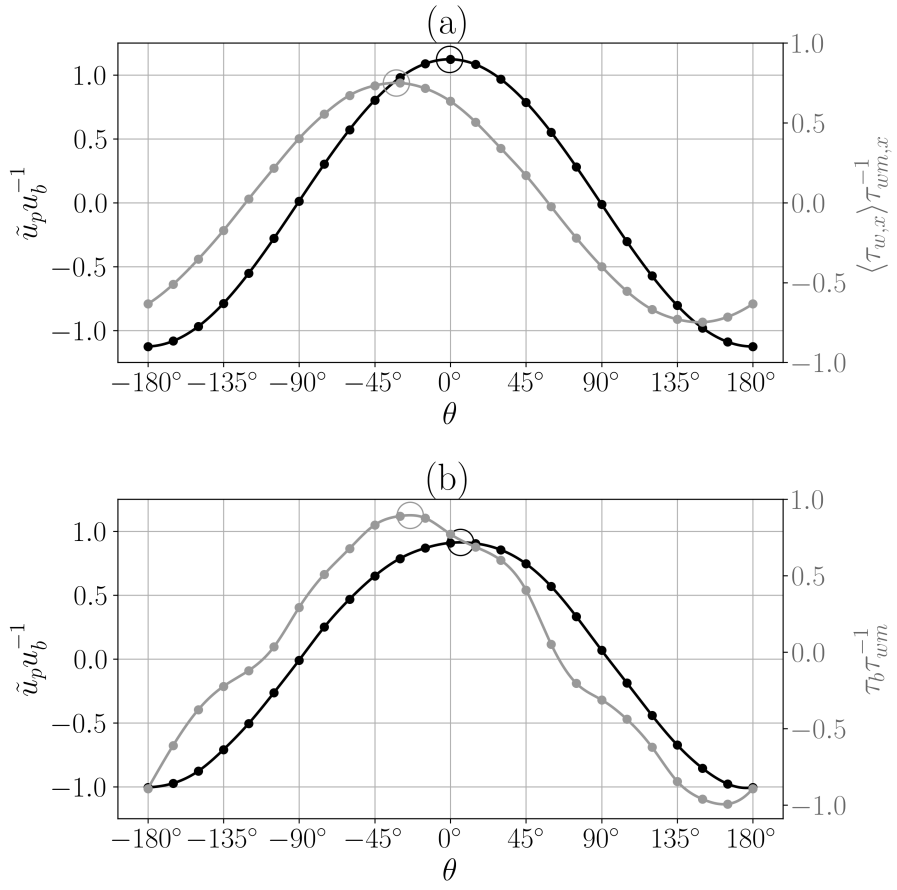

Figure 8: (a) Vectrino measurements of normalized potential velocity (left axis) and normalized bed shear stress (right axis) as a function of wave phase, with the solid line indicating a spline fit. (b) Same as panel (a) for JC76 Trial 1. The maximum value for each variable is denoted by the large open marker, with the phase lag defined as the phase difference between maximum values.

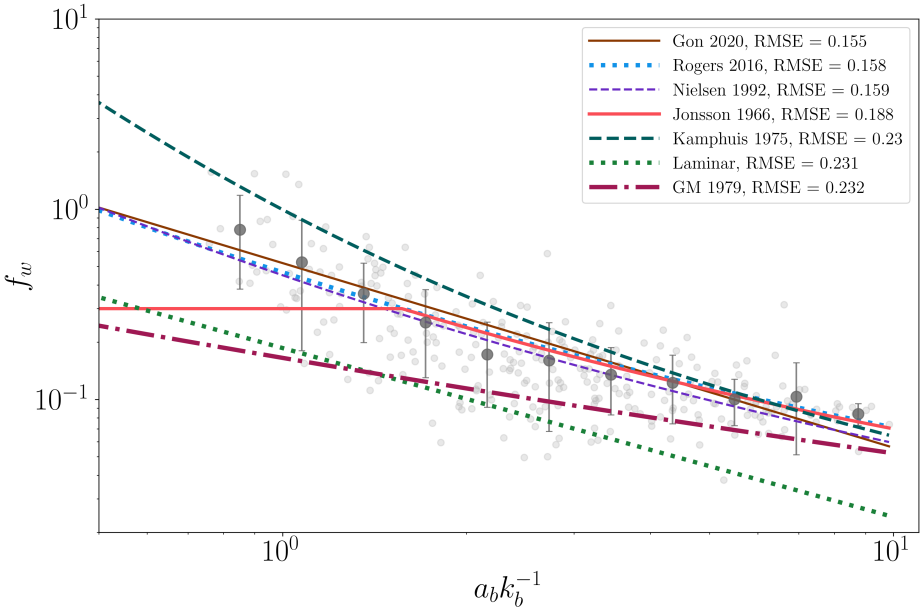

Figure 9: Wave friction factor (Equation 17; bin-averaged with error bars denoting standard deviation, along with raw data as markers) as a function of relative roughness. Lines indicate various wave friction factor parameterizations (Equations 20 - 25), with root-mean-squared error (RMSE) indicated in the legend for each.

to roughness standard deviation. However, if we had used the standard scaling $k_b = 4\sigma_b$, the RMSE would have still been lowest out of all the parameterizations.

Overall, our results indicate that the parameterizations of Gon et al. [16], Rogers et al. [35], and Nielsen [33] are similarly well-suited to represent wave friction in our system. Compared to other studies, this is consistent with some (e.g., Sous et al. [39] found good agreement using Gon et al. [16] and a formulation with coefficients close to Nielsen [33]) but diverges from others (Huang et al. [22] found that GM's f_w parameterization was most accurate), suggesting that results will vary between measurement techniques and the physical system being studied. The Rogers et al. [35] parameterization (and original Swart [42] study that it was based on) was validated using field and laboratory data from a wide range of conditions (e.g., sandy beaches, coral reefs), which may explain its general applicability, while the Gon et al. [16] parameterization was developed using coral reef and rocky shore observations. And though a muddy estuarine sediment bed is not commonly thought of as dynamically similar to a coral reef environment, the combination of large benthic roughness (high k_b) and short-period wind waves (low a_b) in our system means that in terms of relative roughness, the datasets are comparable: both Rogers et al. [35] and Gon et al. [16] included the range $a_b k_b^{-1} \approx 0.1 - 1$ to fit their parameterizations, the same order of magnitude as our minimum $a_b k_b^{-1} \approx 0.75$.

3.3.3 Combined Wave-Current Shear Stress

Figure 10 shows profiles of the combined wave-current shear stress (Equation 14), averaged over all measurement burst periods and divided into time periods of positive and negative mean currents. Aside from the tidally-dependent shift in the profiles towards more positive (flood tide, $\overline{u} > 0$) or more negative (ebb tide, $\overline{u} < 0$) stresses, the vertical structure and phase variability of the combined stress is similar to the purely wave-driven stress depicted in Figure 7a. Flood profiles have higher-magnitude bed stresses, though this is likely a result

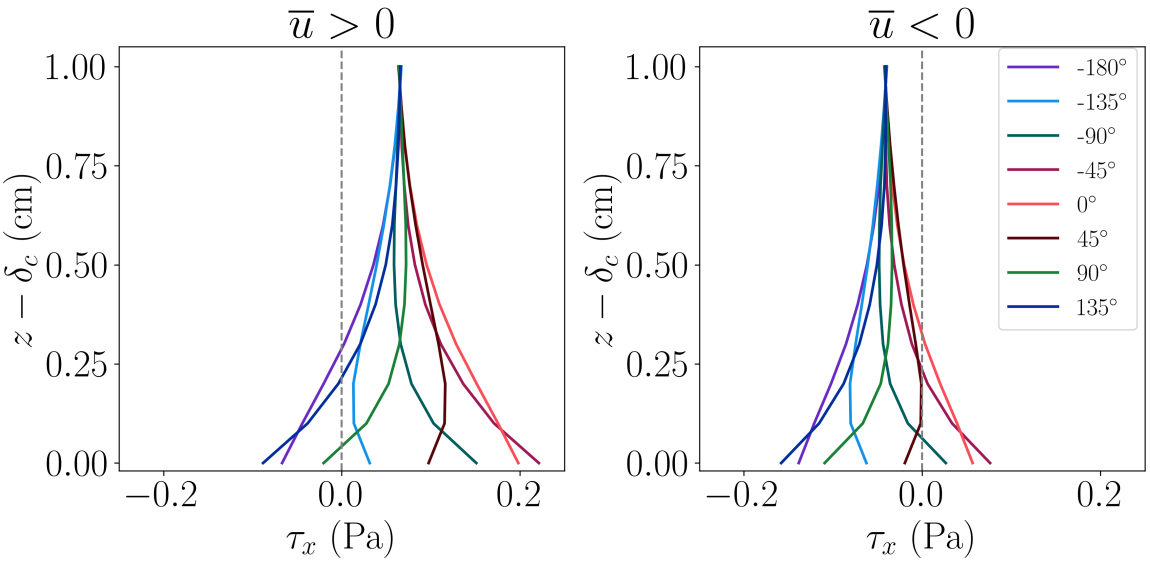

Figure 10: Phase-averaged profiles of combined wave-current shear shear stress (Equation 14), ensemble-averaged during flood tide ($\overline{u} > 0$, left) and ebb tide ($\overline{u} < 0$, right). The dashed vertical line in each panel indicates $\tau_x = 0$ Pa.

of the slightly higher mean velocity on flood tide compared to ebb, rather than an effect of wave-current alignment (which varies as a function of tidal phase). For both flood and ebb tide, the bed shear stress at certain wave phases can oppose the turbulent (current-driven) bed shear stress, with a magnitude approximately equal to the turbulent stress. This phase-dependent sign change could be important for sediment transport, in particular over spatially heterogeneous bed geometry where erodibility may be anisotropic.

3.3.4 Combined Wave-Current Shear Stress Parameterizations

We next evaluate the combined wave-current shear stress parameterizations [18, 41] against our observations, with results shown in Figure 11. Of the two bed shear stress parameterizations, GM is superior both in terms of RMSE and bias. The Styles model tends to underpredict the measured bed stress, particularly during strong wave and current conditions. Nevertheless, the absolute errors are similar and both models show general agreement with our measurements. This is somewhat unexpected considering that GM underestimated the wave friction factor f_w, and by extension the wave-driven bed shear stress (Figure 9). Closer examination of the $|\boldsymbol{\tau_m}|$ prediction error, however, shows that the underestimated wave friction is merely masked in Figure 11 because the tidal component of the shear stress often dominates the signal. This is highlighted in Figure 12 where we plot the GM combined wave-current shear stress residual as a function of bottom wave-orbital velocity u_0. There is a clear negative trend, indicating that the combined stress is predicted with increasing negative bias as wave strength increases (Styles residuals are not shown, but displayed similar behavior).

The results of Figures 11 and 12 could have important consequences for hydrodynamic and sediment transport modelers: namely, GM best parameterizes bottom stress when wave-induced stresses are not the dominant contributor to total (combined wave-current) bed stress. In the limit where the bed shear stress is entirely due to waves, GM underpredicts the stress considerably, which in turn could lead to underpredictions of sediment resuspension and frictional wave dissipation. With that in consideration, we tested a simple modification of the

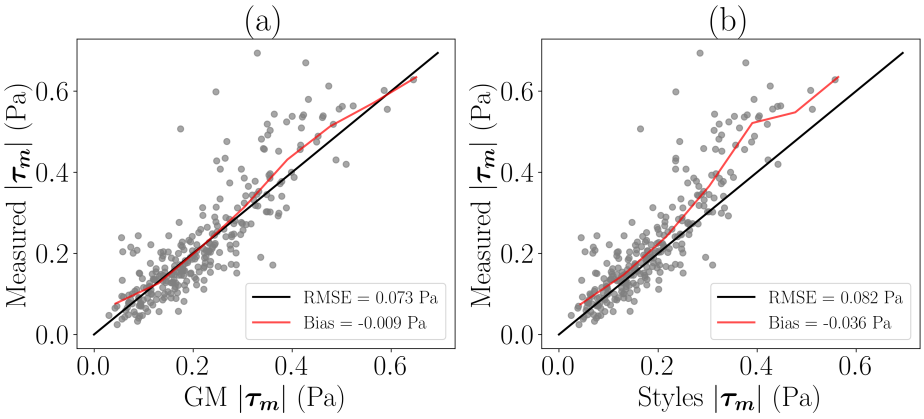

Figure 11: Measured combined wave-current shear stress (vector magnitude of Equation 26b) compared to the (a) Grant and Madsen [18] and (b) Styles et al. [41] parameterizations. The solid black line denotes 1:1 correspondence, while the solid red line denotes the bin-averaged bias.

GM model where the wave friction factor parameterization is replaced by that of Rogers et al. [35] (which performed better against our observations, Figure 9); however, this produced a positive bias in the combined wave-current shear stress with higher error than the standard GM formulation. Nevertheless, our results suggest that a unified approach that implements GM for combined forcing and relaxes to Gon et al. [16] or Rogers et al. [35] when currents are removed may be worth developing, though it is beyond the scope of the current work.

3.4 Suspended Sediment Fluxes

In a previous analysis of this dataset, phase-averaged sediment fluxes were found to be strongly correlated to wave shear stress and combined wave-current shear stress, with only a weak correlation to the turbulent Reynolds stress [11]. Here we examine phase-resolved sediment fluxes, and reevaluate the mechanism by which waves resuspend sediment from the bed.

Figure 13 shows turbulent sediment fluxes $\overline{c'w'}$ over the course of the deployment, separated by flood and ebb tide time periods. Averaging over all heights and wave phases, the sediment flux is net upward ($\overline{c'w'} > 0$) in both current direction cases, but it is approximately 3.5 times larger when $\overline{u} > 0$, likely a consequence of the stronger combined wave-current shear stress during flood tide (Figure 13a).

Despite the stronger flood tide shear stress, there are numerous similarities between the flood and ebb sediment fluxes. Focusing on the canopy region, for instance, we find the strongest upward fluxes near $\theta = -90°$ during both tidal phases. This is coincident with the maximum wave acceleration, slightly leading the maximum shear stress. The alignment of the near-bed erosive fluxes with maximum wave acceleration suggests erosion driven not only by bed shear stress, but by the horizontal wave pressure gradient (Equation 5). This erosion mechanism was examined experimentally by Sleath [38] and measured in the field by Foster et al. [12]. More recently, Marry and Foster [29] showed that strong horizontal pressure gradients correlated to upward vertical gradients of the pore water pressure and momentary liquefaction events within the sediment bed, providing another pathway for bed sediment mobilization. Without direct pressure observations within the bed we cannot confirm whether that latter mechanism was promoting erosion at our site, but the evidence does at least point towards a combined role between bed shear stress and the horizontal wave pressure gradient in driving vertical turbulent sediment fluxes.

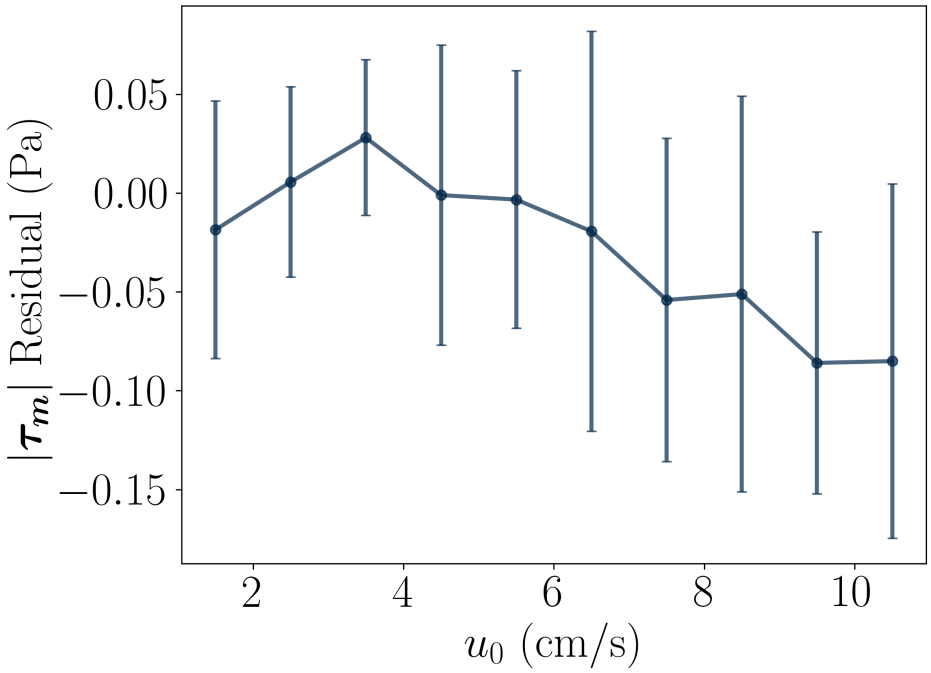

Figure 12: Combined wave-current shear stress residual (predicted - measured) from the GM model, bin-averaged by bottom wave-orbital velocity. Error bars denote the standard deviation about each average.

Further from the bed ($z \approx 0.5$–1.5 cm), there is another strong upward flux region near $\theta = 90°$ during both flood and ebb, aligned with the maximum wave deceleration and leading the largest magnitude negative shear stress. This could be another instance of horizontal pressure gradients and shear acting in concert to erode sediment, though given the vertical positions of the flux maxima, the sediment appears to be sourced from above the canopy rather than the sediment bed itself. This could happen if, for example, a high-concentration fluid mud layer develops over the ≈ 1 cm closest to the bed due to wave-induced sediment resuspension.

To explore the influence of the wave pressure gradient on erosion, we estimated a Sleath number,

$$S = \frac{\rho_0 \partial_t \tilde{u}_p}{g\,(\rho_s - \rho_0)}, \tag{28}$$

where $\rho_s = 1300$ kg/m^3 is the bed sediment density consistent with Egan et al. [10]. This value is denser than the fluid mud limit but significantly less dense than sand, which has been the focus of most prior work evaluating Sleath-like erosion [1]. We estimated S using the maximum velocity acceleration, and an absolute $|S|$ using the magnitude of the minimum velocity deceleration during each measurement burst. Against these Sleath numbers we compared the nondimensional sediment flux $\overline{c'w'}\,(\rho_s u_*)^{-1}$, where $u_* = (\tau_{m,x}\rho_0^{-1})^{1/2}$ is the friction velocity associated with the maximum combined wave-current bed shear stress during each measurement burst. Nondimensionalizing the flux by u_* helps to isolate the effect of wave acceleration independent of wave shear stress. For positive accelerations, we compared S to the maximum sediment flux in the canopy layer during the wave phase where S was maximized in order to identify fluxes like those at $\theta = -90°$ in Figure 13c. Analogously for decelerations, we compared $|S|$ to the maximum sediment flux above the canopy layer during the wave phase where $|S|$ was maximized in order to identify fluxes like those at $\theta = 90°$ in

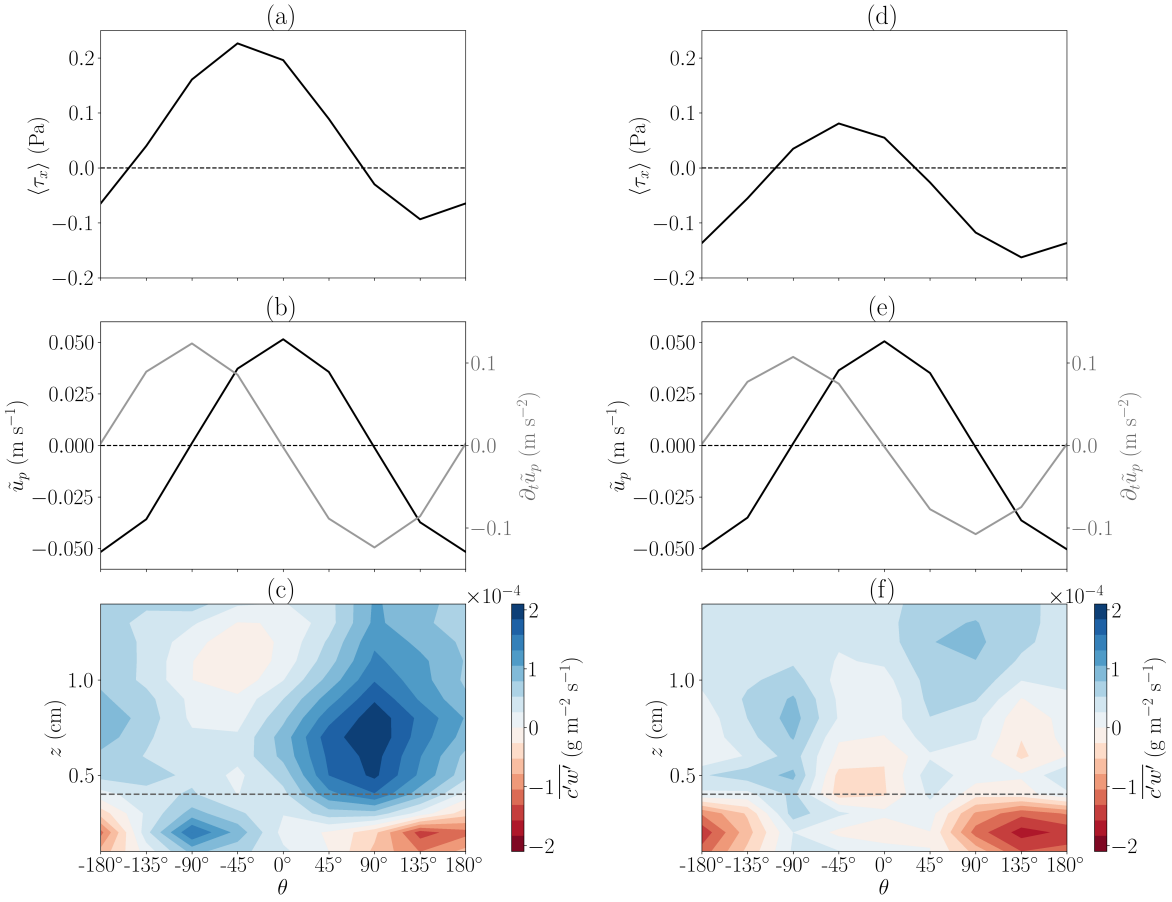

Figure 13: (a) Combined wave-current bed shear stress, (b) potential velocity (black line, left axis) and acceleration (gray line, right axis), and (c) turbulent sediment flux contours averaged over all flood tide time periods. Panels (d-f) show the same data for ebb tide. The black dashed line in panels (c) and (f) indicates the approximate canopy height.

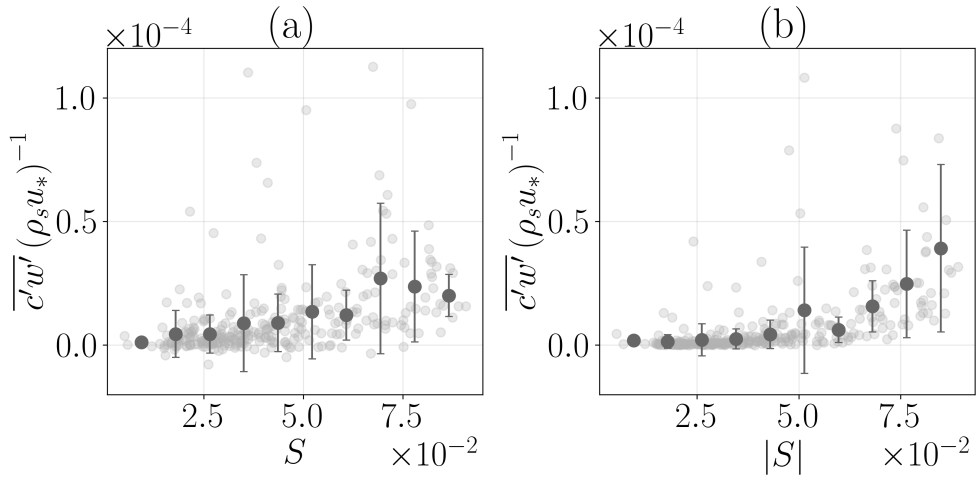

Figure 14: Nondimensional turbulent sediment flux as a function of Sleath Number (Equation 28). In panel (a), S is calculated using the maximum wave acceleration over all phases for a given measurement burst period, while the sediment flux is the maximum value within the canopy layer at the phase corresponding to maximum wave acceleration. Panel (b) shows the same data for maximum wave deceleration and the maximum sediment flux above the canopy layer. Error bars denote standard deviation around the bin-averages.

Figure 13c. This comparison is shown in Figure 14.

For both positive and negative wave pressure gradients, Figure 14 shows an increase in the nondimensional sediment flux with S. The flux increases most near $S \approx 0.06$, which is close to the $S \approx 0.1$ threshold that Foster et al. [12] found. In our case, however, precise thresholds should be treated with caution due to uncertainty in the sediment density, which modifies the magnitude of S. Nevertheless, the trend in Figure 14 supports the assertion that wave pressure gradients have an important role in driving suspended sediment fluxes over the cohesive bed examined here.

Another key feature of Figure 13 are the negative (counter-gradient) fluxes within the canopy region near the bed, aligned with wave phases where the total shear stress is negative. Further from the bed, negative fluxes are visible near $\theta = -45°$ when shear is positive, though these are much weaker in magnitude. The negative fluxes appear during both tidal phases but are more pronounced during ebb tide, which may be a result of the higher magnitude negative shear stress compared to flood. In general, a negative turbulent sediment flux implies that the oft-assumed balance between upward turbulent fluxes and downward mean settling (i.e., Rouse dynamics) does not hold. This could be caused by a number of factors. Lab experiments by Nielsen et al. [34], for instance, found negative fluxes during decelerating wave phases, though our data showed negative fluxes during wave acceleration too. Another study explained counter-gradient buoyancy fluxes in their observations as being controlled by the balance between available potential energy and vertical turbulent kinetic energy, proposing a new nondimensional stratification parameter that delineated between positive flux and negative flux regimes, corresponding to weak and strong stratification, respectively [7]. We estimated their stratification parameter using the Vectrino suspended sediment concentration estimates, but found no correlations with $\overline{c'w'}$ (not shown).

Given the complex bed geometry at our study site and the correlation to negative shear stresses during both flood and ebb tide, another explanation for the negative vertical fluxes could be unresolved horizontal flux divergence, e.g., terms like $\partial_x \overline{u'c'}$ that break the balance

between upward turbulent fluxes and downward settling. For example, roughness geometry may differ upstream and downstream of the Vectrino, leading to horizontally-varying erosion and directional asymmetry in the horizontal sediment flux, with stronger divergence during periods of negative bed shear stress compared to positive bed shear stress. Unfortunately, we are unable to test this hypothesis without horizontally-distributed measurements. Moreover, we could not find observations of turbulent sediment fluxes under similar scenarios in the canopy flow literature, suggesting a more general knowledge gap in our understanding of sediment resuspension in oscillatory flows over large, spatially-varying bottom roughness. It is therefore our hope that these intriguing but ultimately unexplained flux observations inspire further research on that topic.

4 Conclusions

The primary contributions of this work stem from the *in situ* observations of a combined wave-current bottom boundary layer over a rough-bed, resolving both wave phase variability and millimeter spatial scales. We found that vertical profiles of velocity and shear stress were more diffuse than those measured in classic laboratory experiments. We attributed this effect to an extremely rough boundary and proposed a new parameterization for boundary layer depth as a function of relative roughness. We also tested a number of parameterizations for wave-induced and combined wave-current shear stress against our observations. In the purely wave-driven case, we found that the parameterization of Gon et al. [16] performed best in terms of RMSE, though Rogers et al. [35] and Nielsen [33] were very similar. In the combined wave-current case, the parameterization of Grant and Madsen [18] had the lowest error despite underestimating wave-induced shear stress. This suggests that a hybrid bottom boundary layer model that leverages the GM treatment of combined wave-current forcing and combines it with a more accurate wave friction factor parameterization could improve bottom stress estimates in coastal hydrodynamic and sediment transport models.

We next analyzed phase-resolved profiles of turbulent sediment flux, finding that flux maxima occurred during maximum wave acceleration and deceleration. Similar to field studies over sandy beds, this suggests a combined role of wave shear stress and the horizontal wave pressure gradient in resuspending sediment from the bed. We also found downward (counter-gradient) fluxes near the bed during certain wave phases, in particular when the combined wave-current shear stress was negative. We believe that these fluxes were likely a result of horizontal sediment flux variability associated with heterogeneous bed roughness, though we cannot validate that hypothesis with the available data. Overall, these results help to confirm assumptions and parameterizations regarding the structure of the estuarine bottom boundary layer, while raising novel questions about the role of bottom roughness in impacting fluid and sediment dynamics.

Acknowledgements

This work was funded by the U.S. National Science Foundation under Grant OCE-1736668. I thank Stephen Monismith and Oliver Fringer for designing the experiment, and I thank Frank Spada, Kara Scheu, Grace Chang, Craig Jones, Sam McWilliams, Marianne Cowherd, Stephen LaMothe, and Jim Christmann for their assistance planning and carrying out the field work. Finally, I thank the three anonymous reviewers whose comments greatly improved the quality of the manuscript.

Data Availability

All data associated with this manuscript, along with code necessary to process the data and generate the figures can be found at https://github.com/galenegan/wbbl-phase-paper.

Author Contributions

GE: Conceptualization, data processing and archiving, data analysis and visualization, writing.

References

[1] D. Anderson, D. Cox, R. Mieras, J. A. Puleo, and T.-J. Hsu. Observations of wave-induced pore pressure gradients and bed level response on a surf zone sandbar. *Journal of Geophysical Research: Oceans*, 122(6):5169–5193, 2017.

[2] G. K. Batchelor. *An introduction to fluid dynamics*. Cambridge university press, 2000.

[3] A. Brand, J. R. Lacy, K. Hsu, D. Hoover, S. Gladding, and M. T. Stacey. Wind-enhanced resuspension in the shallow waters of south san francisco bay: Mechanisms and potential implications for cohesive sediment transport. *Journal of Geophysical Research: Oceans*, 115(C11), 2010.

[4] J. D. Bricker and S. G. Monismith. Spectral wave–turbulence decomposition. *Journal of Atmospheric and Oceanic Technology*, 24(8):1479–1487, 2007.

[5] J. B. Christoffersen and I. G. Jonsson. Bed friction and dissipation in a combined current and wave motion. *Ocean Engineering*, 12(5):387–423, 1985.

[6] M. Cowherd, G. Egan, S. Monismith, and O. Fringer. Phase-resolved wave boundary layer dynamics in a shallow estuary. *Geophysical Research Letters*, 48(8):e2020GL092251, 2021.

[7] M. A. de Nijs and J. D. Pietrzak. An explanation for salinity-and spm-induced vertical countergradient buoyancy fluxes. *Ocean Dynamics*, 61:497–524, 2011.

[8] G. Egan, M. Cowherd, O. Fringer, and S. Monismith. Observations of near-bed shear stress in a shallow, wave-and current-driven flow. *Journal of Geophysical Research: Oceans*, 124(8):6323–6344, 2019.

[9] G. Egan, G. Chang, G. Revelas, S. Monismith, and O. Fringer. Bottom drag varies seasonally with biological roughness. *Geophysical Research Letters*, 47(15):e2020GL088425, 2020.

[10] G. Egan, A. J. Manning, G. Chang, O. Fringer, and S. Monismith. Sediment-induced stratification in an estuarine bottom boundary layer. *Journal of Geophysical Research: Oceans*, 125(8):e2019JC016022, 2020.

[11] G. Egan, G. Chang, S. McWilliams, G. Revelas, O. Fringer, and S. Monismith. Cohesive sediment erosion in a combined wave-current boundary layer. *Journal of Geophysical Research: Oceans*, 126(2):e2020JC016655, 2021.

[12] D. Foster, A. Bowen, R. A. Holman, and P. Natoo. Field evidence of pressure gradient induced incipient motion. *Journal of Geophysical Research: Oceans*, 111(C5), 2006.

[13] J. Fredsøe. Turbulent boundary layer in wave-current motion. *Journal of Hydraulic Engineering*, 110(8):1103–1120, 1984.

[14] O. B. Fringer, C. N. Dawson, R. He, D. K. Ralston, and Y. J. Zhang. The future of coastal and estuarine modeling: Findings from a workshop. *Ocean modelling*, 143:101458, 2019.

[15] D. K. Fytanidis, M. H. García, and P. F. Fischer. Mean flow structure and velocity–bed shear stress maxima phase difference in smooth wall, transitionally turbulent oscillatory boundary layers: direct numerical simulations. *Journal of Fluid Mechanics*, 928:A33, Dec. 2021. ISSN 0022-1120, 1469-7645. doi: 10.1017/jfm.2021.827. URL https://www.cambridge.org/core/product/identifier/S0022112021008272/type/journal_article.

[16] C. J. Gon, J. H. MacMahan, E. B. Thornton, and M. Denny. Wave dissipation by bottom friction on the inner shelf of a rocky shore. *Journal of Geophysical Research: Oceans*, 125(10):e2019JC015963, 2020.

[17] D. G. Goring and V. I. Nikora. Despiking acoustic doppler velocimeter data. *Journal of hydraulic engineering*, 128(1):117–126, 2002.

[18] W. D. Grant and O. S. Madsen. Combined wave and current interaction with a rough bottom. *Journal of Geophysical Research: Oceans*, 84(C4):1797–1808, Apr. 1979. ISSN 0148-0227. doi: 10.1029/JC084iC04p01797. URL https://agupubs.onlinelibrary.wiley.com/doi/10.1029/JC084iC04p01797.

[19] T. Herbers, S. Elgar, and R. Guza. Directional spreading of waves in the nearshore. *Journal of Geophysical Research: Oceans*, 104(C4):7683–7693, 1999.

[20] M. Hino, M. Kashiwayanagi, A. Nakayama, and T. Hara. Experiments on the turbulence statistics and the structure of a reciprocating oscillatory flow. *Journal of Fluid Mechanics*, 131:363–400, 1983.

[21] T.-W. Hsu and C.-D. Jan. Calibration of businger-arya type of eddy viscosity model's parameters. *Journal of waterway, port, coastal, and ocean engineering*, 124(5):281–284, 1998.

[22] Z.-C. Huang, L. Lenain, W. K. Melville, J. H. Middleton, B. Reineman, N. Statom, and R. M. McCabe. Dissipation of wave energy and turbulence in a shallow coral reef lagoon. *Journal of Geophysical Research: Oceans*, 117(C3), 2012.

[23] I. G. Jonsson. Wave boundary layers and friction factors. In *Coastal engineering 1966*, pages 127–148. 1967.

[24] I. G. Jonsson and N. A. Carlsen. EXPERIMENTAL AND THEORETICAL INVESTIGATIONS IN AN OSCILLATORY TURBULENT BOUNDARY LAYER. *Journal of Hydraulic Research*, 14(1):45–60, Jan. 1976. ISSN 0022-1686, 1814-2079. doi: 10.1080/00221687609499687. URL http://www.tandfonline.com/doi/abs/10.1080/00221687609499687.

[25] J. W. Kamphuis. Friction Factor under Oscillatory Waves. *Journal of the Waterways, Harbors and Coastal Engineering Division*, 101(2):135–144, May 1975. ISSN 0044-8028, 2690-4055. doi: 10.1061/AWHCAR.0000276. URL https://ascelibrary.org/doi/10.1061/AWHCAR.0000276.

[26] J. R. Lacy and L. J. MacVean. Wave attenuation in the shallows of San Francisco Bay. *Coastal Engineering*, 114:159–168, Aug. 2016. ISSN 03783839. doi: 10.1016/j.coastaleng.2016.03.008. URL https://linkinghub.elsevier.com/retrieve/pii/S0378383916300369.

[27] R. J. Lowe, J. L. Falter, M. D. Bandet, G. Pawlak, M. J. Atkinson, S. G. Monismith, and J. R. Koseff. Spectral wave dissipation over a barrier reef. *Journal of Geophysical Research: Oceans*, 110(C4), 2005.

[28] O. S. Madsen. Spectral wave-current bottom boundary layer flows. In *Coastal engineering 1994*, pages 384–398. 1994.

[29] M. Marry and D. Foster. Field observations of hydrostatic pressure deviations in a nearshore sediment bed. *Journal of Geophysical Research: Oceans*, 129(2): e2023JC019891, 2024.

[30] J. M. Mier, D. K. Fytanidis, and M. H. García. Mean flow structure and velocity–bed shear stress maxima phase difference in smooth wall, transitionally turbulent oscillatory boundary layers: experimental observations. *Journal of Fluid Mechanics*, 922:A29, Sept. 2021. ISSN 0022-1120, 1469-7645. doi: 10.1017/jfm.2021.510. URL https://www.cambridge.org/core/product/identifier/S0022112021005103/type/journal_article.

[31] H. M. Nepf. Flow and transport in regions with aquatic vegetation. *Annual review of fluid mechanics*, 44(1):123–142, 2012.

[32] H. M. Nepf. Hydrodynamics of vegetated channels. *Journal of Hydraulic Research*, 50 (3):262–279, 2012.

[33] P. Nielsen. *Coastal bottom boundary layers and sediment transport*, volume 4. World Scientific Publishing Company, 1992.

[34] P. Nielsen, K. Van Der Wal, and L. Gillan. Vertical fluxes of sediment in oscillatory sheet flow. *Coastal Engineering*, 45(1):61–68, Mar. 2002. ISSN 03783839. doi: 10.1016/S0378-3839(01)00043-6. URL https://linkinghub.elsevier.com/retrieve/pii/S0378383901000436.

[35] J. S. Rogers, S. G. Monismith, D. A. Koweek, and R. B. Dunbar. Wave dynamics of a pacific atoll with high frictional effects. *Journal of Geophysical Research: Oceans*, 121 (1):350–367, Jan. 2016. ISSN 2169-9275, 2169-9291. doi: 10.1002/2015JC011170. URL https://agupubs.onlinelibrary.wiley.com/doi/10.1002/2015JC011170.

[36] B. v. Ruessink, T. Van Den Berg, and L. Van Rijn. Modeling sediment transport beneath skewed asymmetric waves above a plane bed. *Journal of Geophysical Research: Oceans*, 114(C11), 2009.

[37] H. Schlichting and K. Gersten. *Boundary-layer theory*. springer, 2016.

[38] J. F. Sleath. Conditions for plug formation in oscillatory flow. *Continental Shelf Research*, 19(13):1643–1664, 1999.

[39] D. Sous, K. Martins, M. Tissier, F. Bouchette, and S. Meulé. Spectral wave dissipation over a roughness-varying barrier reef. *Geophysical Research Letters*, 50(5): e2022GL102104, 2023.

[40] P. R. Spalart and B. S. Baldwin. Direct simulation of a turbulent oscillating boundary layer. In *Turbulent Shear Flows 6: Selected Papers from the Sixth International Symposium on Turbulent Shear Flows, Université Paul Sabatier, Toulouse, France, September 7–9, 1987*, pages 417–440. Springer, 1989.

[41] R. Styles, M. E. Brown, and S. M. Glenn. *An optimized combined wave and current bottom boundary layer model for arbitrary bed roughness*. US Army Engineer Research and Development Center, Coastal and Hydraulics . . . , 2017.

[42] D. H. Swart. Offshore sediment transport and equilibrium beach profiles. *Delft Hydraulics, Pub.*, 131, 1974.

[43] M. Vallikivi, M. Hultmark, and A. J. Smits. Turbulent boundary layer statistics at very high reynolds number. *Journal of Fluid Mechanics*, 779:371–389, 2015.

[44] P. L. Wiberg and C. R. Sherwood. Calculating wave-generated bottom orbital velocities from surface-wave parameters. *Computers & Geosciences*, 34(10):1243–1262, 2008.

[45] Z. You, D. Wilkinson, and P. Nielsen. Velocity distribution in turbulent oscillatory boundary layer. *Coastal engineering*, 18(1-2):21–38, 1992.